Renewable Energy 133 (2019) 284–294

Contents lists available at ScienceDirect

Renewable Energy

journal homepage: www.elsevier.com/locate/renene

Steady and transient operation of an organic Rankine cycle power system

Shuang Cao [a], Jinliang Xu [a, *], Zheng Miao [a], Xiulong Liu [a], Ming Zhang [a], Xuewang Xie [b], Zhi Li [b], Xiaoli Zhao [b], Guihua Tang [c]

[a] The Beijing Key Laboratory of Multiphase Flow and Heat Transfer, North China Electric Power University, Beijing, 102206, China
[b] Hebei Electric Power Design & Research Institute, Shijiazhuang, 050031, Hebei, China
[c] Key Laboratory of Thermo-Fluid Science and Engineering of Ministry of Education, School of Energy & Power Engineering, Xi'an Jiaotong University, Xi'an, Shanxi, 710049, China

ARTICLE INFO

Article history:
Received 4 February 2018
Received in revised form
29 September 2018
Accepted 8 October 2018
Available online 9 October 2018

Keywords:
Organic Rankine cycle
Single screw expander
Steady state
Transient operation
Electric energy quality

ABSTRACT

The Organic Rankine Cycle (ORC) driven by low-grade energy can operate in off-grid mode. Here, we report the steady and transient characteristics of an ORC system. A single screw expander and a synchronous generator convert mechanical power to electricity. A lamp array simulates the variable external loads. The quality parameters including electric frequency, electric power and effective voltage are measured by a power meter. We show that at setting frequency of 50 Hz, the maximum system efficiency can be reached when the external load is not larger than the ORC power capacity. The expander isentropic efficiency is above 80% for the vapor superheating of 5–10 K at expander inlet. A control strategy is proposed to achieve better system performance under varied heat source and environment conditions. By use of residual frequency and adjusting pumping frequency, the vapor pressure at expander inlet can be automatically adjusted to reach the optimal value. Transient tests indicate that the electric quality is insensitive to the step change of external loads and heat/cold sources parameters. The thermohydraulic parameters are self-adapted to the change of external parameters. This work provides a self-adapting strategy for ORC operation at varied heat/cold source parameters.

1. Introduction

The Organic Rankine Cycle (ORC) is a promising technology to utilize various renewable energies, such as solar energy [1–3], biomass energy [4,5], geothermal energy [6,7] and ocean thermal energy [8]. A number of works have been devoted to ORCs from experimental and theoretical aspects. Theoretical works focus on the thermodynamic analysis, selection of working fluids, and control model development [9–14]. Braimakis and Karellas [9] carried out a thermo-economic optimization of two cycle configurations: a standard ORC and a regenerative ORC. The effects of different heat source condition, expander types and working fluids were investigated. Sun et al. [10] showed the importance of operational parameters such as evaporation temperature, condensation temperature and vapor superheating at expander inlet on system performance. Chagnon-Lessard et al. [11] investigated performance and economical optimization of subcritical and trans-critical ORCs at different operational parameters. The working fluids also has a significant impact on thermodynamic and economic performance of ORCs. Xu and Yu [12] found that the critical temperature of working fluids can be the sole criterion to reach higher thermal efficiency.

Experimental studies are focused on the development and measurement of small-scale ORCs (1–10 kW power capacity) [15–17]. Yamamoto et al. [15] designed and tested a micro-turbine with R123 as the working fluid. The maximum shaft power was measured to be 0.15 kW. Zhou et al. [16] investigated the effects of evaporating pressure, heat source temperature and vapor superheating on power output. Yang et al. [17] examined the effects of pressure drop, vapor superheating and condenser temperature on overall system performance, indicating the negative contribution of condenser temperature on power output and thermal efficiency.

How to improve the power-to-electricity conversion efficiency is one of the important issues in ORCs. In previous studies, an asynchronous generator is driven by an expander to generate

* Corresponding author.
E-mail address: xjl@ncepu.edu.cn (J. Xu).

https://doi.org/10.1016/j.renene.2018.10.044
0960-1481/

electricity [18–22]. The asynchronous generator can adapt to the variation of expander rotating speed in a wide range. However, due to the increased internal irreversible losses caused by the output current hysteresis effect, the power-to-electricity conversion efficiency is only about 40–60% [21,22]. In contrast to the asynchronous generator, a synchronous generator exhibits a higher power-to-electricity conversion efficiency of 90–98% [23–25]. Because the power-to-electricity conversion efficiency is influenced by the expander rotating speed, it is important to keep the optimal rotating speed of expander when a synchronous generator is used [26].

Several studies have been reported on the ORC control theory and strategy [27]. Quoilin et al. [28] developed the static and dynamic models to control an ORC. The results showed that the predictive control strategy based on the steady-state optimization model is better than the control strategy based on other models. Manente et al. [29] noted that the practical operation condition may be different from the design condition. They developed an off-design model to optimize the operation parameters so that the electricity output can be maximum at varied environment temperatures and geofluid temperature. Das et al. [30] dealt with the automatic generation control to overcome frequency excursion under the condition of mismatch between power generation and external load. The performance of a PSO (particle swarm optimization) optimized controller is better than a GA (genetic algorithm) optimized counterpart in terms of settling time and parameter overshoot due to frequency deviation. Shi et al. [31] established an ADRC (Active Disturbance Rejection Control) based control approach. The control system includes sub-systems of an outer sub-loop controller for evaporating pressure, a control allocator to allocate mass flow rate of exhaust gas, and an inner sub-loop controller for valve adjustments. Zhang et al. [32,33] proposed a multi-variables-feedback control strategy to reach the maximum energy utilization degree when waste heat is used as the heat source. The results show that the exhaust gas can be utilized, and the constrained predictive controller can achieve satisfactory performance for set-point tracking and disturbance rejection. Recently, Ziviani et al. [34] developed a control-oriented steady state cycle model which is based on their empirical experiment correlations. Using the model, a feed-forward control strategy was proposed by changing the pump speed to achieve the optimal evaporating pressure under given external loads. They emphasized that their control strategy is not suitable for varied heat source conditions.

Even though different control strategies and models have been proposed for ORC, these models are too idealized for practical operation. For example, the efficiencies of pump and expander are assumed to be constant during operation. The static models of evaporator and condenser are also used for simplification. Thus, practical models suitable for the dynamic operation are expected in the future.

Few experimental studies of ORC control system are reported. Kang [35] integrated a simple control system into an ORC system. The proportional integral derivative (PID) controller was used to maintain pressure and vapor superheating at expander inlet and condenser temperature at the desired values. The factors influencing the ORC performance were discussed. Usman et al. [36] used a sliding pressure control strategy to satisfy the varying load demand by changing evaporation pressure using a proportional-integral (PI) algorithm. An improved scheme based on the Proportional Integral (PI), feed-forward and lead-lag compensator was tested for identical operating conditions and load disturbances. Torregrosa et al. [37] used an adaptive PID based control system to consider effects of high inertia of boiler and condenser and low inertia of pump and expander on the ORC performance.

We note that, available studies focused on the control of ORC system in a short time-scale of minutes. However, due to the system thermal inertia, parameter excursions may occur to deviate from the setting values in a longer time-scale such as hours. The dynamic performance in both short and long time-scales is not investigated sufficiently. Most importantly, available control studies involved the ORC itself, not including the power-to-electricity conversion process. For practical operation, the electric energy quality parameters such as electric power frequency (f_{ele}), electric power (W_{ele}) and effective voltage ($\overline{U}$) are important for users. No studies are reported to control the electric energy quality parameters.

The objective of this paper is to experimentally study the control of electric energy quality parameters under varied heat source and environment conditions. Not only the thermohydraulic parameters such as pressures and temperatures, but also the electric energy quality parameters, are monitored and controlled. We found that electric energy quality is influenced by the match between the ORC power capacity and the external load. When the external load is equal to or smaller than ORC power capacity, one can reach the 50 Hz electric frequency, otherwise, the 50 Hz frequency cannot be ensured. The step change of heat source and cooling water parameters and external loads has almost no effect on the electric energy quality, which is attractive for industrial applications.

2. Experimental setup

2.1. ORC power generation system

Fig. 1 shows the ORC system with R245fa as working fluid. The heat capacity of heat source (thermal oil) is 100 kW and the rated expander shaft power is 6.0 kW. The ORC system contains three sub-systems: thermal oil loop (red color), ORC loop (black color) and cooling water loop (blue color). They are described as follows.

2.1.1. The ORC unit

Fig. 2 shows the three-dimensional drawing and the photo of the ORC unit, including an organic fluid circulation loop, an expander, a power generator with its monitor system, and a programmable logic controller (PLC) control system.

The organic fluid circulation loop consists of a liquid tank, an organic fluid pump, a mass flow meter, an evaporator, an expander and a condenser. A hydraulic diaphragm pump circulates the organic fluid, having a rated outlet pressure of 1.5 MPa and a flow rate of 1.9 m^3/h. The mass flow rate was controlled by a frequency

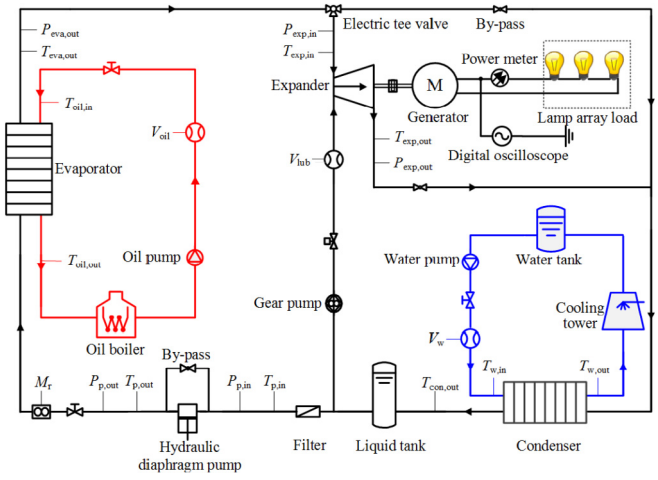

Fig. 1. The ORC system.

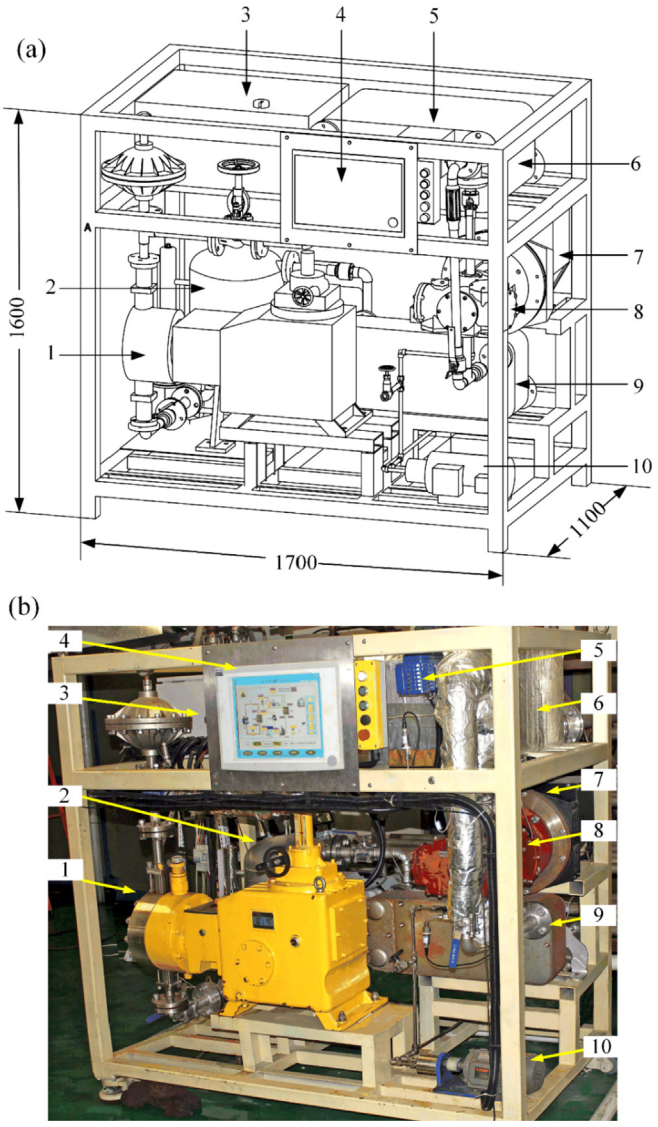

Fig. 2. Three-dimensional drawing (a) and photo (b) of the ORC unit (1: working fluid pump, 2: liquid tank, 3: PLC, 4: IPC, 5: electric tee valve, 6: evaporator, 7: power generator, 8: expander, 9: condenser, 10: gear pump).

converter. The mass flow rate m_r was measured by a Coriolis mass flow meter. The evaporator and condenser are two plate heat exchangers, having heat transfer areas of 35.9 m^2 and 12.3 m^2, respectively. At expander entrance, an electric tee valve either operates the expander or by-passes the expander by switching the organic vapor to flow in different tube-lines. A three-phase synchronous generator converts the expander shaft power into electricity. The power generator had a maximum power output of 11 kW, a rated rotating speed of 3000 rpm (corresponding to 50 Hz frequency) and a line voltage of 400 V. The generator was connected coaxially with the expander by an elastic coupling. Thus, the generator and expander had identical rotating speeds. A twelve halogen lamps array directly consumed the electricity generated by the power generator. The lamp array had a 10.5 kW maximum capacity. Table 1 shows the parameters of main components.

The liquid charging process is paid attention here. Because non-condensable gas is important to affect the system performance, it is necessary to remove the non-condensable gas in the closed ORC system before liquid is charged into the system. At the liquid tank bottom of the ORC system, a tube line connects the liquid tank and a vacuum pump separated by a valve, and another tube line connects the liquid tank and an organic liquid bottle, also separated by a valve. Initially, the vacuuming process is performed with the corresponding valve open but with the other valve off. The vacuuming process lasted 1 h. Then, the corresponding valve is turned off, and the other valve is switched on. The organic liquid is automatically flowed from the high pressure-bottle to the liquid tank of the ORC system.

During operation, the power generator provided the electric power W_{ele}, which was directly measured by an electric power meter. The electric power based thermal efficiency is calculated as $\eta_{ele} = W_{ele}/Q_r$. The net system efficiency is $\eta_{net,ele}=(W_{ele}\text{-}W_p)/Q_r$, where W_p is pumping power measured by a frequency converter, and Q_r is heat received by ORC, which is $Q_r = m_r(h_{eva,out}\text{-}h_{eva,in})$, $h_{eva,out}$ and $h_{eva,in}$ are R245fa enthalpies based on the measured temperature and pressure at evaporator outlet and inlet, respectively. The pressure ratio and expander isentropic efficiency are

$$R = P_{exp,in}/P_{exp,out} \tag{1}$$

$$\eta_{exp,s} = \frac{h_{exp,in} - h_{exp,out}}{h_{exp,in} - h_{exp,out,s}} \tag{2}$$

where $P_{exp,in}$ and $P_{exp,out}$ are the expander inlet and outlet pressures, $h_{exp,in}$ and $h_{exp,out}$ are the R245fa enthalpies based on measured temperature and pressure at expander inlet and outlet, $h_{exp,out,s}$ is the expander outlet enthalpy based on isentropic expansion.

2.1.2. The thermal oil loop

The thermal oil was heated by an electric heater with a 100 kW capacity. Due to on-off operation mode of the PID, the oil temperature is quasi-stable with a small oscillation in a range of ±5 °C. The flow rate of thermal oil was circulated by an oil pump and could be controlled by an adjustment valve. The oil volume flow rate (V_{oil}) was measured by a flow meter. The oil temperatures entering and leaving ORC are $T_{oil,in}$ and $T_{oil,out}$, respectively. The heat supplied by the thermal oil is

$$Q_{oil} = V_{oil}\rho_{oil}C_{p,oil}(T_{oil,in} - T_{oil,out}) \tag{3}$$

where ρ_{oil} and $C_{p,oil}$ are the oil density and specific heat, which are determined by the average temperature of evaporator inlet and outlet.

2.1.3. The cooling water loop

A cooling tower with a maximum cooling capacity of 150 kW was installed outdoor to extract heat from the condenser. The heat was finally dissipated to the environment. During operation, the slow change of environment temperatures caused the variation of cooling water temperature in a long time-scale of hours. A valve adjusted the cooling water flow rate, which was measured by a turbine flow meter. The cooling water temperatures entering and leaving ORC were measured.

2.2. The single screw expander

For the expander, the mechanical configuration, power capacity, isentropic efficiency and flow rate influence the ORC performance. The single screw expander balances the axial force by a main rotor and can operate in a wide range of power capacities [38]. In this paper, the single screw expander was modified from a commercial single screw compressor, having a power capacity of 7.5 kW. Fig. 3 shows the internal structure of the single screw expander. A pair

Table 1
Parameters of main components.

Instruments	Parameters
Piston pump	Rated outlet pressure: 1.5 MPa, rated flow rate: 1.9 m^3/h
Evaporator	Plate heat exchanger, heat transfer area: 35.9 m^2
Condenser	Plate heat exchanger, heat transfer area: 12.3 m^2
Expander	Power capacity: 7.5 kW
Generator	Rated power output:11 kW, rated rotating speed:3000 rpm
Thermal conduction oil boiler	Heating capacity: 100 kW
Cooling tower	Cooling capacity: 150 kW

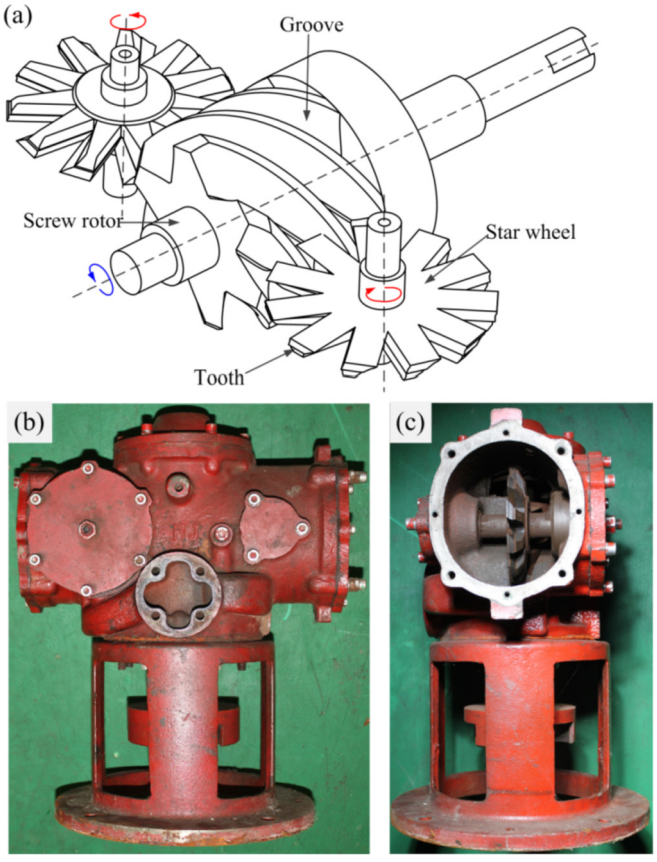

Fig. 3. Single screw expander (a: the screw coupling with two star wheels, b: front view of the expander, c: side view of the expander for internal structure).

of star wheels is coupled with the screw rotor, symmetrically. The rotor had six grooves and a star wheel had eleven teeth. The coupling between the rotor and the two star-wheels forms two vapor expansion channels at any time. The two star-wheels work simultaneously to generate mechanical power. The expander operation needs lubricant. Different from other studies [38,39], the R245fa liquid, instead of oil, was directly injected into the expander from a liquid tank by a gear pump (see Fig. 1). The lubricant flow rate was about 2% of the main flow rate, maximally. During normal operation, if the expander is sufficiently lubricated, the lubricant flow rate can be decreased or turned off. The expander back-pressure is smaller compared to the oil lubrication method. The organic fluid lubrication does not need an oil-water separator and the ORC system can be simplified.

2.3. The lamp array

Fig. 4 shows the lamp array to simulate the electric load. The lamp array was connected with the power generator by the star connection. The lamp array consisted of four groups. The first group had three lamps with a 0.5 kW capacity for each lamp. The other group had three lamps with a 1 kW capacity for each lamp. Any combination of the four groups, can be connected with the power generator by an air switch, simulating different loads applied to ORC. The lamp array consumed load was measured by a three-phase multi-function power meter. In order to dynamically monitor the electric energy quality, a parallel four-channel digital oscilloscope (type RIGOL-DS1054Z) was connected in the electric loop to display real-time phase voltage. In such a way, the dynamic phase voltage for all the three phases and the phase angle between any two phases can be simultaneously displayed and recorded by a computer. It is noted that a differential probe (mutual inductor) converts a high voltage (~400 V scale) to a low voltage according to a specific conversion ratio, which was set as 100:1 in this study. Thus, the digital oscilloscope is electrically insulated from the high voltage. The match between the ORC power capacity and the electric load capacity influences the electric frequency. The power capacity was about 6 kW for current ORC system. The standard 50 Hz electric frequency can be reached if the external load is smaller than 6.0 kW, but the electric frequency is decreased if the external load is larger than 6.0 kW.

2.4. The adaptive control system

Fig. 5 shows the adaptive control principle. For ORC off-grid operation, various components and parameters are coupled with each other. The heat source parameters (heat carrier fluid temperature and flow rate) and the electric load influence the pressure

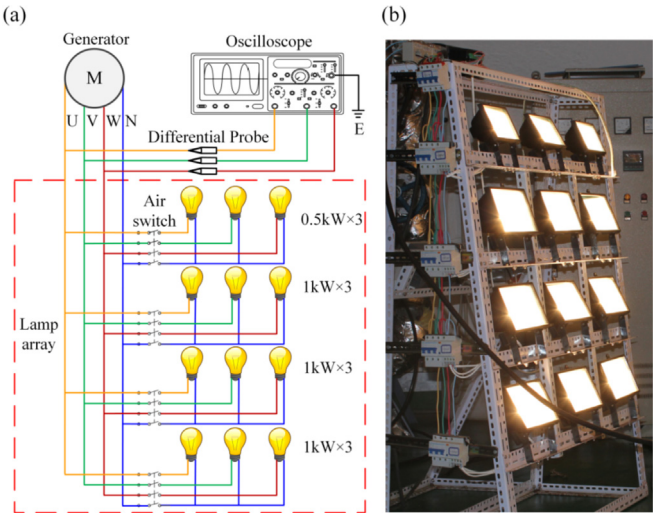

Fig. 4. Lamp array load system (a: the electric connection, b: running of the lamp array load).

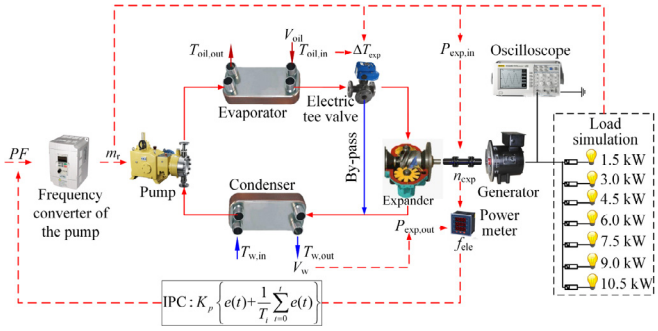

Fig. 5. Working principle of control system.

and vapor superheating at expander inlet. The cooling water temperature and flow rate affect the expander back-pressure. The combined effect of heat source and cooling medium influences the expander performance. The voltage and frequency of the power generator are dependent on expander rotating speeds.

Because the 50 Hz frequency is acceptable for any off-grid utilization, the control system should achieve a 50 Hz electric power at varying conditions. The control system consists of three subsystems (see Fig. 5): a main electric control part (red color), a lamp array load part (black color) and a by-pass part (blue color). If the load capacity is identical to or smaller than the ORC power capacity, the control system ensures the 50 Hz electric frequency. If the load capacity is larger than the ORC power capacity, the output frequency is less than 50 Hz. By system control, if the expander speed is larger than 3000 rpm (corresponding to 50 Hz), the by-pass line is automatically activated to by-pass part of the organic flow rate to maintain the 50 Hz frequency. If the expander speed is larger than 3600 rpm, the vapor flow rate entering expander is thoroughly closed and the total flow rate is by-passed to protect the expander.

The power generator frequency (f_{set}) is set to a specific value such as 50 Hz. The real-time frequency is measured and recorded as $f_{ele}(t)$. The residual frequency is

$$e(t) = f_{ele}(t) - f_{set} \tag{4}$$

The Industrial Personal Computer (IPC) gave the following signal as

$$\Delta u(t) = K_P\left\{e(t) + \frac{1}{\tau_i}\sum_{t=0}^{t} e(t)\right\} \tag{5}$$

where K_p is the proportional constant and τ_i is the integration time. The pump frequency of the R245fa fluid is adjusted based on Eq. (5). The R245fa flow rate is linearly related to the pumping frequency. It is important to select suitable K_p and τ_i. Usually, K_p is in the range of 0.2–1.3 for heat engine control. The selection of τ_i is dependent on the cycle period of varying heat source ($\tau_{heat\ source}$) and the system thermal inertia: $\tau_i \sim \tau_{heat\ source}$. In this study, τ_i equals to 200 s. If τ_i is too small, the adjustment process is fast to cause the system over-control. If τ_i is too long, the adjustment process needs a longer time to reach the steady state. A single adjustment signal $\Delta u(t)$ is generated within each integration time duration τ_i. The pressures and temperatures at various state points, cycling mass flow rate and electric power are measured (see Table 2). The expander isentropic efficiency is calculated based on Eq. (2). Thermal efficiency, electric power based thermal efficiency and net system efficiency are defined as the enthalpy difference across the expander, the electric power, and the electric power subtracting the pumping power, divided by the total absorption heat, respectively. The uncertainties of these parameters are determined by the error transmission theory [40]. The expander isentropic efficiency, electric power based thermal efficiency and net system efficiency had accuracies of 4.76%, 3.96% and 4.12%, respectively.

3. Results and discussion

3.1. Steady state operation performance

The steady state operation refers to the whole system operating at quasi-stable temperature and flow rate of the heat source and the cooling water. For each run, the electric load and power frequency (corresponding to expander rotating speed) are specified. Here, the effects of power frequencies and electric loads on the ORC thermohydraulic parameters are examined. Table 3 shows the 24 runs. The expander rotating speeds and electric loads covered the range of 1500–3000 rpm and 1.5–6.0 kW, respectively. Fig. 6 shows various parameters dependent on expander rotating speeds (n_{exp}) and electric loads at a 120.3 °C thermal oil temperature entering ORC with an oscillation amplitude of 3.4 °C.

3.1.1. R245fa mass flow rate

When expander rotating speed and/or electric load are increased, the mass flow rate of R245fa is increased to increase vapor pressure at expander inlet to adapt the increase of external loads (see Fig. 6a).

3.1.2. Expander performance

With increase of expander speeds and/or external loads, the vapor temperature and superheating at expander inlet are decreased, but the pressures at expander inlet and outlet are increased (see Fig. 6b–e). The faster rise of pressures at expander inlet than those at outlet slightly increases the pressure ratios across the expander (see Fig. 6f). At expander inlet, the vapor temperature and pressure are coupled with each other. We note that an evaporator consists of a preheating section with single-phase liquid flow, an evaporation section with two-phase flow, and a superheating section with single-phase vapor flow. For a specific evaporator, the total heat transfer area is given. The variations of fluid pressure and temperature change the heat transfer area for each of the three sections. With increase of pressures, the saturation temperature is increased but the latent heat of evaporation is decreased. Therefore, the rise of vapor pressure elongates the preheating section, but shorten the evaporation section and the superheating section. This effect decreases the vapor temperature and superheating at expander inlet.

3.1.3. Electric power and efficiencies

More electric power is generated with increases of expander speeds and/or external loads (see Fig. 6g). The slopes of electric powers against expander speeds are larger at larger external loads. Similar phenomenon is found to the pumping power (Fig. 6h). The electric power based thermal efficiencies, η_{ele}, and the net thermal efficiencies, $\eta_{net,ele}$, are increased with increases of expander speeds and/or external loads (see Fig. 6i–j). The ORC system exists the "best" match among the expander speeds, the external loads and the ORC thermal capacity. Both η_{ele} and $\eta_{net,ele}$ reach maximum at 6 kW external load and 50 Hz electric frequency, having $\eta_{ele} = 6.19\%$ and $\eta_{net,ele} = 4.67\%$.

The coupling effect between expander speeds and external loads is investigated, focusing on four runs: $f_{ele} = 25.7$ Hz and 49.2 Hz at 1.5 kW external load, $f_{ele} = 24.6$ Hz and 44.4 Hz at 6.0 kW external load (see Fig. 6i). The corresponding *T-s* cycles are shown in Fig. 7a–d. At an external load of 1.5 kW, the electric power is increased from 0.45 kW at $f_{ele} = 25.7$ Hz to 1.52 kW at $f_{ele} = 49.2$ Hz

Table 2
Major parameters, instruments and uncertainties.

Parameters	Instruments	Uncertainties	Response time
Temperature (°C)	KMQXL-040G-6	±0.5 °C	1 s
Pressure (kPa)	CYT-103	0.2%	1 ms
R245fa mass flow rate (kg/h)	DMF-1	0.2%	/
Conductive oil flow rate (m^3/h)	YD-LBL-65	0.5%	/
Cooling water flow rate (m^3/h)	YD-LWGY-50	0.5%	/
Lubricant flow rate (m^3/h)	YD-LWGY-10	0.5%	/
Electric power (kW)	AKW91110	0.5%	10 ms
Phase voltage (V)	AKW91110	0.2%	10 ms
Electric frequency (Hz)	AKW91110	0.2%	10 ms
Pumping power (kW)	ACS510	2%	5 ms
Real-time voltage (V)	RIGOL-DS1054Z	0.5%	500 ps
By-pass (on/off)	JLQ945PPL-25P	/	25s
Temperature signals (°C)	FPO-TC	0.3%	/
Pressure and flow rate signals (mA)	FPRRAD	1%	/

Table 3
Running parameters for steady-state experiment.

Run	$T_{oil,in}$ (°C)	V_{oil} (m^3/h)	$T_{w,in}$ (°C)	V_w (m^3/h)	n_{exp} (rpm)	*Load* (kW)
1	120.6 ± 2.8	12.65 ± 0.21	23.2 ± 0.2	7.32 ± 0.13	1536 ± 48	1.5
2	120.6 ± 2.9	12.58 ± 0.30	23.7 ± 0.4	7.26 ± 0.05	2014 ± 56	1.5
3	120.7 ± 3.4	12.45 ± 0.37	24.6 ± 0.7	7.24 ± 0.04	2494 ± 50	1.5
4	120.1 ± 3.5	12.80 ± 0.41	28.1 ± 1.0	7.17 ± 0.06	2949 ± 107	1.5
5	120.5 ± 2.4	12.96 ± 0.31	28.5 ± 0.4	7.17 ± 0.04	1563 ± 51	3.0
6	120.6 ± 3.0	13.05 ± 0.40	28.9 ± 0.5	7.15 ± 0.05	1988 ± 88	3.0
7	120.0 ± 3.6	13.20 ± 0.50	29.5 ± 0.6	7.36 ± 0.07	2496 ± 34	3.0
8	119.8 ± 3.7	12.90 ± 0.40	31.4 ± 1.1	7.09 ± 0.10	2965 ± 149	3.0
9	120.8 ± 3.6	13.15 ± 0.44	24.0 ± 0.2	6.98 ± 0.13	1540 ± 94	4.5
10	120.6 ± 3.6	13.23 ± 0.32	24.7 ± 0.7	7.03 ± 0.09	2067 ± 103	4.5
11	120.0 ± 3.7	13.19 ± 0.45	26.8 ± 0.9	7.14 ± 0.05	2490 ± 102	4.5
12	119.5 ± 3.5	12.94 ± 0.32	28.7 ± 0.7	6.97 ± 0.06	2913 ± 195	4.5
13	120.5 ± 3.5	13.18 ± 0.50	25.2 ± 0.5	6.99 ± 0.09	1474 ± 68	6.0
14	120.5 ± 3.7	12.86 ± 0.33	26.7 ± 0.8	6.91 ± 0.06	2040 ± 60	6.0
15	119.5 ± 4.0	12.82 ± 0.38	30.0 ± 1.7	7.02 ± 0.04	2443 ± 79	6.0
16	120.0 ± 3.2	12.95 ± 0.47	32.8 ± 1.4	6.94 ± 0.05	2664 ± 100	6.0
17	105.1 ± 2.8	13.15 ± 0.49	22.3 ± 0.2	6.95 ± 0.10	1534 ± 84	1.5
18	105.2 ± 2.6	12.96 ± 0.52	22.8 ± 0.3	7.04 ± 0.12	2041 ± 41	1.5
19	105.3 ± 3.0	12.88 ± 0.24	24.1 ± 0.8	7.18 ± 0.06	2443 ± 55	1.5
20	104.9 ± 3.7	13.08 ± 0.30	26.3 ± 1.1	7.13 ± 0.05	2965 ± 125	1.5
21	105.0 ± 3.0	13.12 ± 0.39	27.3 ± 0.6	7.02 ± 0.07	1473 ± 63	3.0
22	105.0 ± 3.1	13.03 ± 0.36	27.5 ± 0.6	7.16 ± 0.05	2046 ± 60	3.0
23	104.7 ± 3.5	13.05 ± 0.38	29.1 ± 1.0	7.06 ± 0.06	2553 ± 87	3.0
24	105.2 ± 3.4	12.90 ± 0.31	30.6 ± 0.8	7.16 ± 0.08	2850 ± 124	3.0

(see Fig. 7a–b). Fig. 7a–c identifies the positive effect of external loads on electric powers. The electric frequency and external load strongly influence the vapor superheating at expander inlet to influence ORC performance. The lower electric frequency and external load elevate the vapor superheating at expander inlet to decrease η_{ele} to 1.52% (see Fig. 7a), which is consistent with the classical thermodynamics regarding the effect of vapor superheating on thermal efficiencies [9]. Alternatively, the higher electric frequency and external load decrease the vapor superheating at expander inlet to 7.5 °C, elevating the efficiency to $\eta_{ele} = 6.19\%$ (see Fig. 7d). The classical thermodynamics yields higher thermal efficiency at the saturation vapor state. However, for practical ORC operation, the saturation vapor entrains small liquid droplets, which attack expander walls to deteriorate the expander performance. This effect explains why the saturation vapor at expander inlet does not exhibit the maximum efficiency in this study. Droplets do not exist when the vapor superheating is increased to a value such as 7.5 °C to improve the system performance. This finding is consistent with our previous study [41].

3.2. System response to the step change of various parameters

System response to the step change of external loads, heat source and cooling water is examined here. The system operates in an automatic control mode. When a step parameter change occurs, the system transfers from a steady state to another one within a time duration. In the following figures, white and pink regions refer to the transition stage and the steady stage respectively. Two types of parameters are classified: the thermohydraulic parameters of pressure *P*, temperature *T* and flow rate *m*, and the electric parameters of effective voltage $\overline{U}$ and electric frequency f_{ele}.

3.2.1. Response to the step change of external loads

Fig. 8 shows the system response when the external loads are sharply changed from 1.5 kW to 3.0 kW, and from 3.0 kW to 4.5 kW. When the external load is switched from a level to another one, the thermohydraulic parameters follow the change of external load. The step increase of external load raises the pumping frequency *PF* and the R245fa mass flow m_r, but lowers the vapor superheating at expander inlet. $\overline{U}$ and f_{ele} are two important parameters to

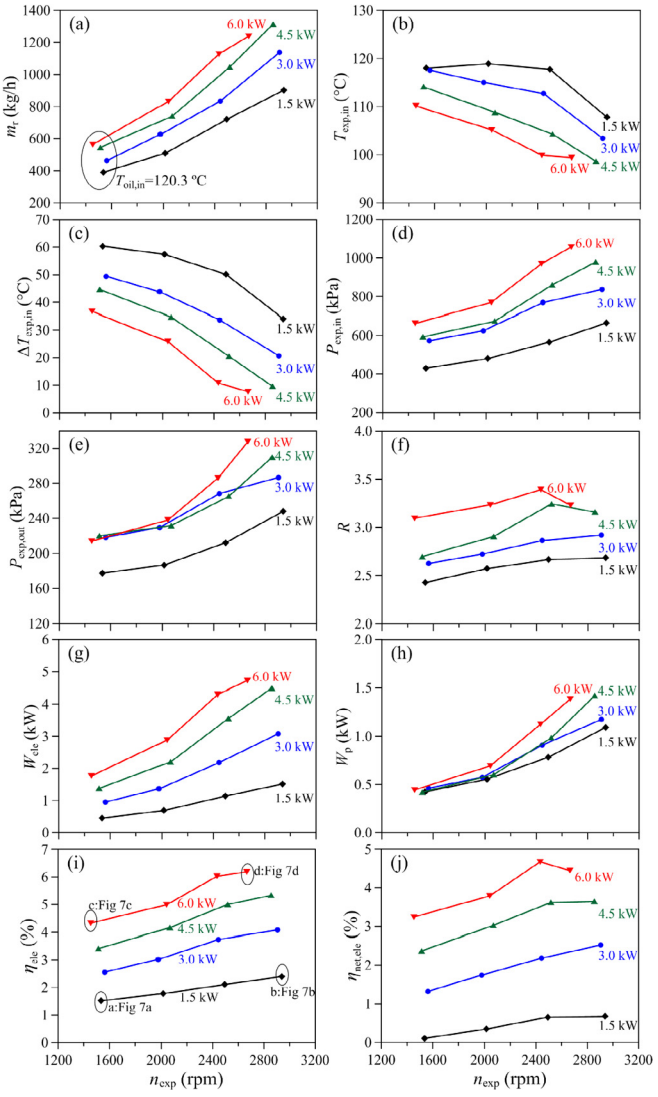

Fig. 6. Steady state parameters at $T_{oil,in} = 120.3 \pm 3.4\,°C$, $V_{oil} = 12.93 \pm 0.38\,m^3/h$ and $V_w = 7.11 \pm 0.23\,m^3/h$ (the variance values such as 3.4 °C means the oscillation amplitude, not the measurement uncertainty.).

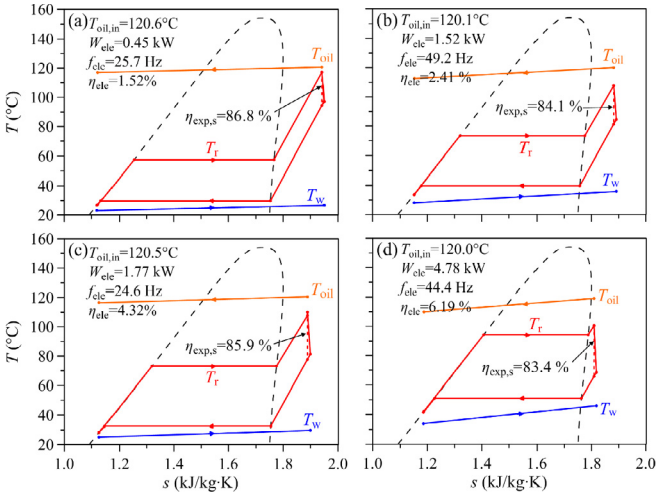

Fig. 7. The *T-s* cycles corresponding to points a, b, c and d in Fig. 6i.

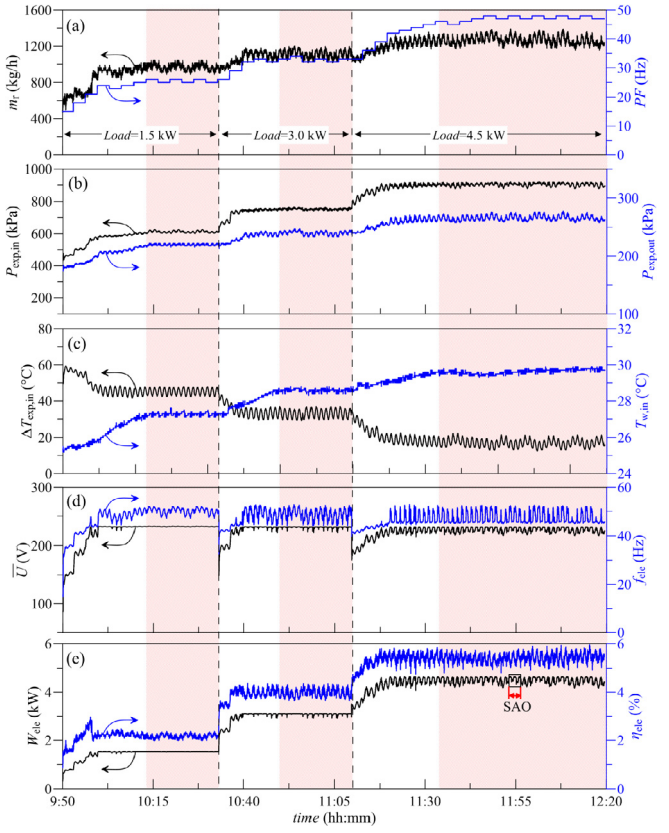

Fig. 8. System performance response to the step change of external loads at $T_{oil,in} = 120.1 \pm 4.5\,°C$, $V_{oil} = 12.84 \pm 0.44\,m^3/h$, $V_w = 7.42 \pm 0.09\,m^3/h$ and $n_{exp} = 3000$ rpm.

characterize the electric energy quality. The step change of external load sharply decreases $\overline{U}$ and f_{ele}, but they are recovered to the initial levels in 10 min (see Fig. 8d). $\overline{U}$ and f_{ele} are self-adapted to keep constant values when the disturbance of external loads appears.

The transition from a steady state to another steady state lasts about 10 min to adapt the external load disturbance. The small amplitude oscillation (SAO) with short cycle period is superimposed on the long-term operation curves. The SAO in Fig. 8e is further enlarged in Fig. 9 to show the dynamic curve in detail, giving a cycle period of 200 s. The electric powers are very stable and the electric power frequencies f_{ele} are oscillating in a range of 45.3–52.5 Hz. The SAO is caused by steady oscillation of thermal oil temperatures by using the on-off periodic heating mode. The cycle period of thermal oil temperatures determines the cycle period of electric powers. The oscillation amplitude of thermal oil temperatures influences the amplitude of electric frequencies. Our finding shows stable electric energy quality for the external load disturbance, but the electric energy quality is influenced by the slow transition of heat source parameters. Thus, a stable heat source is recommended to keep better electric energy quality.

Our synchronous generator had a rated frequency of 50 Hz, corresponding to 3000 rpm expander rotating speed. Fig. 10 presented the transition between different expander speeds. The real electric frequency, f_{ele}, follows the step change of expander speeds. The effective voltage, $\overline{U}$, and the electric power, W_{ele}, are different for different expander speeds. The change of effective voltages limits the electric energy application. Thus, the variable frequency operation mode is not recommended.

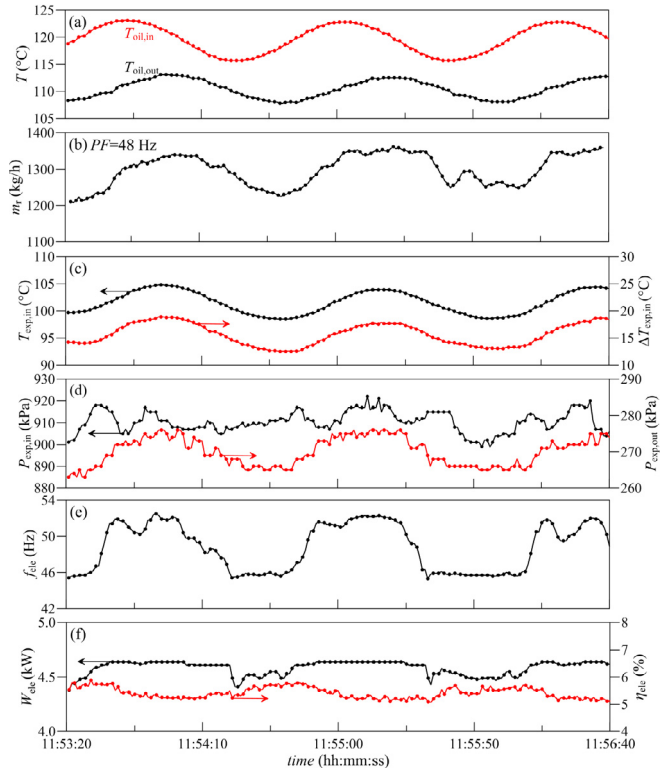

Fig. 9. Parameters in small amplitude oscillation (SAO) at a short-time scale in Fig. 8.

3.2.2. Response to the step change of heat source and cooling water parameters

Figs. 11–13 demonstrate the system response to the step changes of temperatures and flow rates of thermal oil and flow rates of cooling water. Various parameters are coupled and self-adapted with each other to determine the system performance. The electric energy quality is characterized by $\overline{U}$, f_{ele} and W_{ele}, which are important for users.

It is observed that these parameters are not sensitive to the step changes of heat source and cooling water parameters. When the inlet oil temperatures decrease from 120.3 °C to 104.8 °C, $\overline{U}$, f_{ele} and W_{ele} almost do not change (see Fig. 11). Similar phenomena are observed for the step change of heat source and cooling water parameters (see Figs. 12 and 13). Clearly, our ORC system self-adapts pressure, temperature and flow rate to achieve the standard 50 Hz electric frequency.

The insensitivity behavior is further analyzed here. Figs. 11 and 12 show the system response to the step change of oil temperature and flow rate. The decrease of thermal oil temperature/flow rate reduces the enthalpy difference across the evaporator outlet and inlet. The heat received from thermal oil equals to the mass flow rate of organic fluid multiplying by the enthalpy difference across the evaporator outlet and inlet. The combined effect of decreased enthalpy difference and increased flow rate yields similar heat absorption from the heat source. Thus, the electric efficiency η_{ele} is not changed for the step change of thermal oil parameters.

The insensitivity behavior is also analyzed from the expander

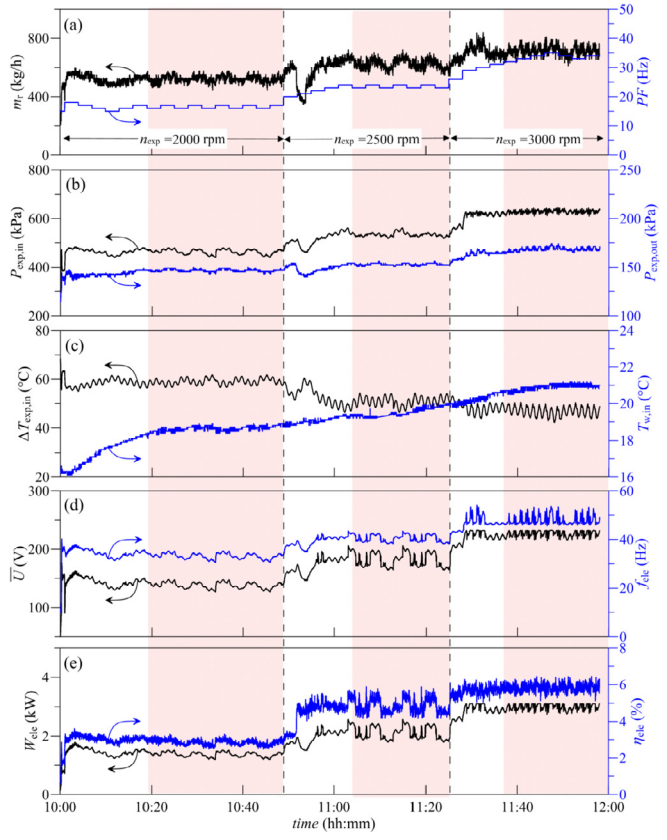

Fig. 10. System performance response to the step change of expander speeds at $T_{oil,in}$ = 119.0 ± 3.3 °C, V_{oil} = 13.05 ± 0.44 m^3/h, V_w = 7.31 ± 0.12 m^3/h and *Load* = 3.0 kW.

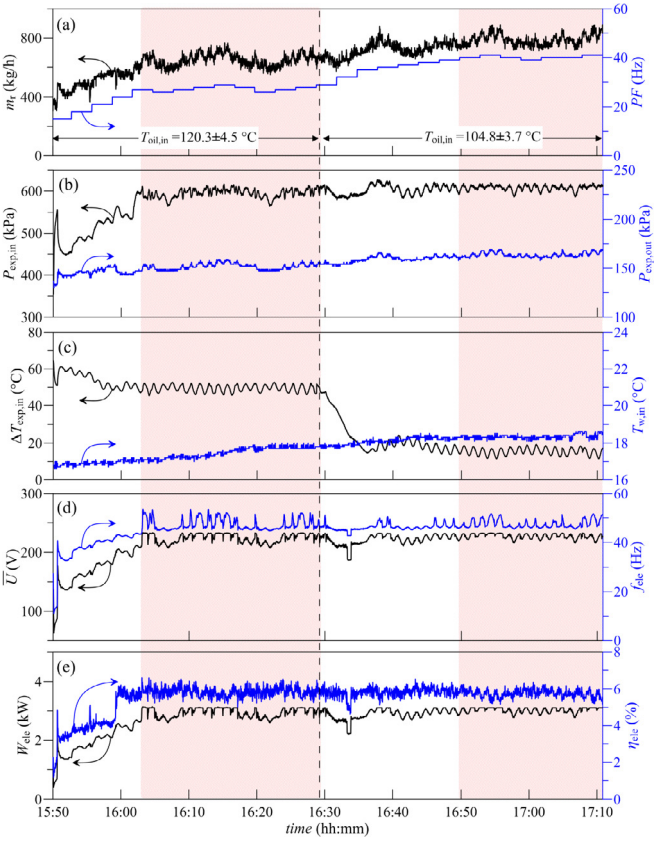

Fig. 11. System performance response to the step change of thermal oil temperatures entering ORC at V_{oil} = 13.09 ± 0.49 m^3/h, V_w = 7.08 ± 0.13 m^3/h, *Load* = 3.0 kW and n_{exp} = 3000 rpm.

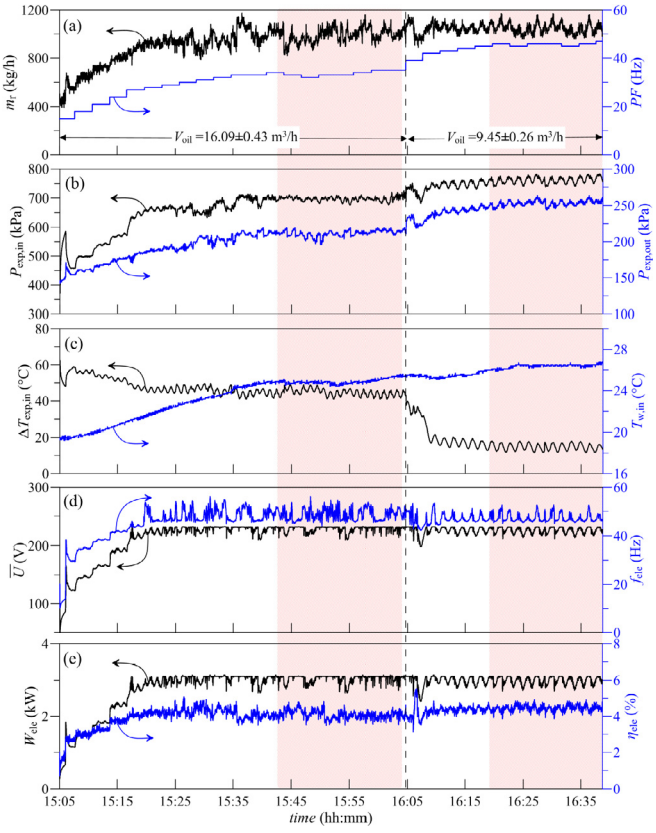

Fig. 12. System performance response to the step change of oil flow rates at $T_{oil,in} = 121.8 \pm 3.8$ °C, $V_w = 7.39 \pm 0.2$ m³/h, *Load* = 3.0 kW and $n_{exp} = 3000$ rpm.

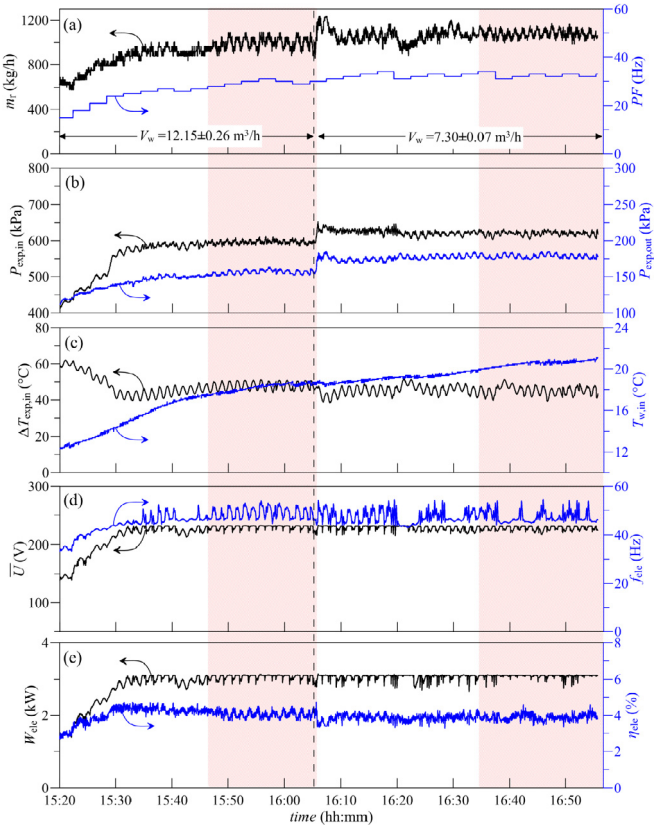

Fig. 13. System performance response to the step change of flow rates of cooling water at $T_{oil,in} = 119.9 \pm 4.1$ °C, $V_{oil} = 13.18 \pm 0.29$ m³/h, *Load* = 3.0 kW and $n_{exp} = 3000$ rpm.

performance point of view. The decreased heat transfer ability of evaporator has positive and negative effects on the expander performance. The increased flow rate and decreased vapor superheating at expander inlet increase mechanical power, behaving positive effect on expander. Alternatively, the decreased fluid temperature in expander increases fluid leakage to worsen expander isentropic efficiency, behaving negative effect on expander. The two effects are competed with each other to yield a constant power output.

The mechanism to keep constant electric energy quality parameters is analyzed. Fig. 11 shows the system transition between two steady states of $T_{oil,in} = 120.3$ °C and 104.8 °C. Fig. 14 plots the *T-s* and *T-Q* curves at the steady states. When the oil temperature is decreased, the control system increases flow rate of organic fluid (m_r) from 604.7 kg/h at $T_{oil,in} = 120.3$ °C to 771.1 kg/h at $T_{oil,in} = 104.8$ °C. The thermal oil temperature determines heat transfer rate of the evaporator. The higher oil temperature 120.3 °C results in a longer superheating section in the evaporator to cause a vapor superheating of 49.4 °C. The decrease of oil temperature and increase of organic fluid flow rate obviously shortens the superheating section in evaporator, yielding a gentle vapor superheating of 15.6 °C. The increased flow rate of organic fluid increases overall heat transfer coefficient in the evaporator, elevating the heat absorption from 47.1 kW to 51.5 kW, even though $T_{oil,in}$ is decreased. We note that the m_r rise also increases heat dissipation to environment via the condenser, which is 42.5 kW at $T_{oil.in} = 120.3$ °C and 45.6 kW at $T_{oil,in} = 104.8$ °C. Based on energy conservation, the mechanical power is determined by the difference between heat absorption from heat source and heat dissipation to environment. Therefore, when the heat source temperature is decreased, the increased flow rate of organic fluid

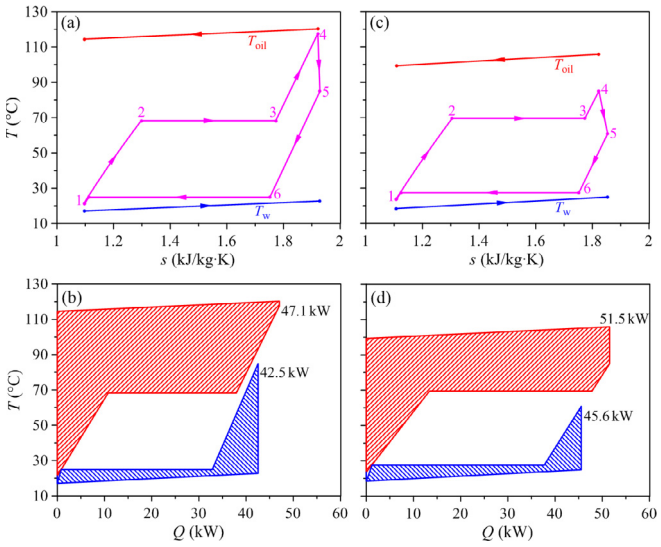

Fig. 14. *T-s* and *T-Q* curves when thermal oil inlet temperatures are changed (a and b for $T_{oil,in} = 120.3$ °C, $m_r = 604.7$ kg/h, $\eta_{exp,s} = 87.2\%$, $W_{ele} = 2.83$ kW, $\eta_{ele} = 6.03\%$; c and d for $T_{oil,in} = 104.8$ °C, $m_r = 771.1$ kg/h, $\eta_{exp,s} = 60.6\%$, $W_{ele} = 2.94$ kW, $\eta_{ele} = 5.73\%$).

simultaneously elevates the heat absorption from heat source, and the heat dissipation to environment, providing quasi-constant output work for ORC user (see Fig. 14). Similar analysis can be performed regarding the disturbance effect of other parameters on the system performance.

4. Conclusions

We provide a control strategy for ORC systems in off-grid operation mode. For such operation, the electric quality parameters such as electric frequency and effective voltage are important for ORC users. In this study, a single screw expander and a synchronous generator are included in the system. It is shown that the ORC system achieves better performance when the external load is not larger than the ORC power capacity, under which the standard 50 Hz electric frequency can be reached. The expander isentropic efficiency attains maximum for the vapor superheating of 5–10 K at expander inlet. The classical equilibrium-thermodynamics assumes no liquid droplets in the saturation vapor. For practical ORC operation, the saturation vapor may entrain liquid droplets. These droplets attack expander walls to deteriorate the expander performance. Thus, a specific vapor superheating is necessary to eliminate the droplets effect during the vapor expansion. The transient tests demonstrate that the electric parameters are not sensitive to the variations of heat source and cold source parameters by using the proposed control strategy. The mechanism for the self-adaptive characteristics of the ORC system is analyzed.

Acknowledgement

The study was supported by the National Key R&D Program of China (2017YFB0601801), and the Natural Science Foundation of China (51776064).

References

[1] E. Bellos, C. Tzivanidis, Parametric analysis and optimization of an Organic Rankine Cycle with nanofluid based solar parabolic trough collectors, Renew. Energy 114 (2017) 1376–1393.
[2] R. Rayegan, Y.X. Tao, A procedure to select working fluids for Solar Organic Rankine Cycles (ORCs), Renew. Energy 36 (2011) 659–670.
[3] M. Marion, I. Voicu, A.L. Tiffonnet, Wind effect on the performance of a solar organic Rankine cycle, Renew. Energy 68 (2014) 651–661.
[4] G. Taljan, G. Verbič, M. Pantoš, M. Sakulin, L. Fickert, Optimal sizing of biomass-fired Organic Rankine Cycle CHP system with heat storage, Renew. Energy 41 (2012) 29–38.
[5] B.F. Tchanche, G. Lambrinos, A. Frangoudakis, G. Papadakis, Low-grade heat conversion into power using organic Rankine cycles – a review of various applications, Renew. Sustain. Energy Rev. 15 (2011) 3963–3979.
[6] F. Heberle, M. Preißinger, D. Brüggemann, Zeotropic mixtures as working fluids in Organic Rankine Cycles for low-enthalpy geothermal resources, Renew. Energy 37 (2012) 364–370.
[7] Y.J. Baik, M. Kim, K.C. Chang, Y.S. Lee, H.K. Yoon, A comparative study of power optimization in low-temperature geothermal heat source driven R125 transcritical cycle and HFC organic Rankine cycles, Renew. Energy 54 (2013) 78–84.
[8] M.H. Yang, R.H. Yeh, Analysis of optimization in an OTEC plant using organic Rankine cycle, Renew. Energy 68 (2014) 25–34.
[9] K. Braimakis, S. Karellas, Integrated thermoeconomic optimization of standard and regenerative ORC for different heat source types and capacities, Energy 121 (2017) 570–598.
[10] W.Q. Sun, X.Y. Yue, Y.H. Wang, Exergy efficiency analysis of ORC (organic Rankine cycle) and ORC based combined cycles driven by low-temperature waste heat, Energy Convers. Manag. 135 (2017) 63–73.
[11] N. Chagnon-Lessard, F. Mathieu-Potvin, L. Gosselin, Geothermal power plants with maximized specific power output: optimal working fluid and operating conditions of subcritical and transcritical Organic Rankine Cycles, Geothermics 64 (2016) 111–124.
[12] J.L. Xu, C. Yu, Critical temperature criterion for selection of working fluids for subcritical pressure Organic Rankine cycles, Energy 74 (2014) 719–733.
[13] G.B. Abadi, K.C. Kim, Investigation of organic Rankine cycles with zeotropic mixtures as a working fluid: advantages and issues, Renew. Sustain. Energy Rev. 73 (2017) 1000–1013.
[14] D. Jolevski, O. Bego, P. Sarajcev, Control structure design and dynamics modelling of the organic Rankine cycle system, Energy 121 (2017) 193–204.
[15] T. Yamamoto, T. Furuhata, N. Arai, K. Mori, Design and testing of the organic Rankine cycle, Energy 26 (2001) 239–251.
[16] N.J. Zhou, X.Y. Wang, Z. Chen, Z.Q. Wang, Experimental study on organic Rankine cycle for waste heat recovery from low-temperature flue gas, Energy 55 (2013) 216–225.
[17] S.C. Yang, T.C. Hung, Y.Q. Feng, C.J. Wu, K.W. Wong, K.C. Huang, Experimental investigation on a 3 kW organic Rankine cycle for low-grade waste heat under different operation parameters, Appl. Therm. Eng. 113 (2017) 756–764.
[18] Y.R. Lee, C.R. Kuo, C.C. Wang, Transient response of a 50 kW organic Rankine cycle system, Energy 48 (2012) 532–538.
[19] K.C. Pang, S.C. Chen, T.C. Hung, Y.Q. Feng, S.C. Yang, K.W. Wong, et al., Experimental study on organic Rankine cycle utilizing R245fa, R123 and their mixtures to investigate the maximum power generation from low-grade heat cycle system, Energy 133 (2017) 636–651.
[20] N. Chaiyat, Y. Wakaiyang, X. Inthavideth, Enhancement efficiency of organic Rankine cycle by using sorption system, Appl. Therm. Eng. 122 (2017) 368–379.
[21] J.C. Hsieh, B.R. Fu, T.W. Wang, Y. Cheng, Y.R. Lee, J.C. Chang, Design and preliminary results of a 20-kW transcritical organic Rankine cycle with a screw expander for low-grade waste heat recovery, Appl. Therm. Eng. 110 (2017) 1120–1127.
[22] L. Guillaume, A. Legros, A. Desideri, V. Lemort, Performance of a radial-inflow turbine integrated in an ORC system and designed for a WHR on truck application: an experimental comparison between R245fa and R1233zd, Appl. Energy 186 (2017) 408–422.
[23] U. Muhammada, M. Imran, D.H. Lee, B.S. Park, Design and experimental investigation of a 1 kW organic Rankine cycle system using R245fa as working fluid for low-grade waste heat recovery from steam, Energy Convers. Manag. 103 (2015) 1089–1100.
[24] L. Li, Y.T. Ge, X. Luo, S.A. Tassou, Experimental investigations into power generation with low gradewaste heat and R245fa organic Rankine cycles (ORCs), Appl. Therm. Eng. 115 (2017) 815–824.
[25] S. Eyerer, C. Wieland, A. Vandersickel, H. Spliethoff, Experimental study of an ORC (organic Rankine cycle) and analysis of R1233zd-E as a drop-in replacement for R245fa for low temperature heat utilization, Energy 103 (2016) 660–671.
[26] L. Pierobon, E. Casati, F. Casella, F. Haglind, P. Colonna, Design methodology for flexible energy conversion systems accounting for dynamic performance, Energy 68 (2014) 667–679.
[27] P. Linke, A.I. Papadopoulos, P. Seferlis, Systematic methods for working fluid selection and the design, integration and control of organic Rankine cycles—a review, Energies 8 (2015) 4755–4801.
[28] S. Quoilin, R. Aumann, A. Grill, A. Schuster, V. Lemort, H. Spliethoff, Dynamic modeling and optimal control strategy of waste heat recovery organic Rankine cycles, Appl. Energy 88 (2011) 2183–2190.
[29] G. Manente, A. Toffolo, A. Lazzaretto, M. Paci, An organic Rankine cycle off-design model for the search of the optimal control strategy, Energy 58 (2013) 97–106.
[30] D.C. Das, N. Sinha, A.K. Roy, Automatic generation control of an organic Rankine cycle solar–thermal/wind–diesel hybrid energy system, Energy Technol. 2 (2014) 721–731.
[31] R.Q. Shi, T.Q. He, J. Peng, Y.J. Zhang, W.L. Zhuge, System design and control for waste heat recovery of automotive engines based on organic Rankine cycle, Energy 102 (2016) 276–286.
[32] J.H. Zhang , W, F. Zhang, G.L. Hou, F. Fang, Dynamic modeling and multivariable control of organic Rankine cycles in waste heat utilizing processes, Comput. Math. Appl. 64 (2012) 908–921.
[33] J.H. Zhang, Y.L. Zhou, R. Wang, J.L. Xu, F. Fang, Modeling and constrained multivariable predictive control for ORC (organic Rankine cycle) based waste heat energy conversion systems, Energy 66 (2014) 128–138.
[34] D. Ziviani, S. Gusev, S. Lecompte, E.A. Groll, J.E. Braun, W.T. Horton, et al., Optimizing the performance of small-scale organic Rankine cycle that utilizes a single-screw expander, Appl. Energy 189 (2017) 416–432.
[35] S.H. Kang, Design and experimental study of ORC (organic Rankine cycle) and radial turbine using R245fa working fluid, Energy 41 (2012) 514–524.
[36] M. Usman, M. Imran, D.H. Lee, B.S. Park, Experimental investigation of off-grid organic Rankine cycle control system adapting sliding pressure strategy under proportional integral with feed-forward and compensator, Appl. Therm. Eng. 110 (2017) 1153–1163.
[37] A. Torregrosa, J. Galindo, V. Dolz, L. Royo-Pascual, R. Haller, J. Melis, Dynamic tests and adaptive control of a bottoming organic Rankine cycle of IC engine using swash-plate expander, Energy Convers. Manag. 126 (2016) 168–176.
[38] D. Ziviani, S. Gusev, S. Lecompte, E.A. Groll, J.E. Braun, W.T. Horton, et al., Characterizing the performance of a single-screw expander in a small-scale organic Rankine cycle for waste heat recovery, Appl. Energy 181 (2016) 155–170.
[39] B. Lei, W. Wang, Y.T. Wu, C.F. Ma, J.F. Wang, L. Zhang, et al., Development and experimental study on a single screw expander integrated into an organic Rankine cycle, Energy 116 (2016) 43–52.
[40] C. Tropea, A.L. Yarin, J.F. Foss, Springer Handbook of Experimental Fluid Mechanics, vol. 1, 2007.
[41] X.F. Yang, J.L. Xu, Z. Miao, J.H. Zou, C. Yu, Operation of an organic Rankine cycle dependent on pumping flow rates and expander torques, Energy 90 (2015) 864–878.

Nomenclature

C_p: specific heat capacity at constant pressure kJ/(kg·K)
e: residual frequency Hz

f: frequency Hz
h: enthalpy kJ/kg
K_p: proportional constant
Load: load capacity kW
m: mass flow rate kg/h
n: rotating speed rpm
P: pressure Pa
PF: pump frequency Hz
Q: heat transfer rate kW
R: expander inlet and outlet pressure ratio
time: time s
T: temperature °C
ΔT: temperature superheating °C
U: voltage V
Δu: adjustment signal
V: volume flow m^3/h
W: power kW

Greek symbols

ρ: density kg/m^3
η: efficiency
τ_i: integral time s

Subscripts

con: condenser
enth: enthalpy difference
ele: electric power
eva: evaporator
exp: expander
in: inlet
net: net
out: outlet
oil: thermal oil
p: pump
r: working fluid (R245fa used in this study)
s: isentropic process
set: setting value
shaft: shaft power
t: real-time
w: cooling water